Angewandte Chemie International Edition

Angewandte International Edition Chemie

How to cite: *Angew. Chem. Int. Ed.* **2026**, 65, e7073224
doi.org/10.1002/anie.7073224

RESEARCH ARTICLE Hot Paper

Tandem Photocatalytic H_2O_2 Production and In Situ Upgrading Enabled by Docking and Locking Engineered Covalent Organic Frameworks

Qiang Xue[1,2] | Jiehua Ding[2] | Zhendong Luo[2,3] | Yunyang Qian[4] | Peng Jin[2,3] | Hai-Long Jiang[4] | Feng Wang[1,2,3] | Xukai Zhou[2,3]

[1]School of Chemistry, Dalian University of Technology, Dalian, P. R. China | [2]State Key Laboratory of Catalysis, Dalian Institute of Chemical Physics, Chinese Academy of Sciences, Dalian, P. R. China | [3]University of Chinese Academy of Sciences, Beijing, P. R. China | [4]Hefei National Research Center for Physical Sciences At the Microscale, Department of Chemistry, University of Science and Technology of China, Hefei, P. R. China

Correspondence: Yunyang Qian (yyq94@mail.ustc.edu.cn) | Xukai Zhou (xkzhou@dicp.ac.cn)

Received: 5 January 2026 | **Revised:** 20 March 2026 | **Accepted:** 24 March 2026

Keywords: alkene difuncationalization | covalent organic frameworks | H_2O_2 synthesis | in situ utilization | tandem photocatalysis

ABSTRACT

Photocatalytic H_2O_2 generation is hindered by low concentrations and energy-intensive purification, posing major barriers to practical application. Herein, a tandem catalytic strategy that integrates H_2O_2 generation with its in situ utilization in organic synthesis is reported to overcome these constraints. Covalent organic frameworks (COFs) engineered through a "docking and locking" strategy provide an ideal platform for enabling such tandem transformations. The optimized TTPh–OH COF delivers benchmark H_2O_2 production rates of 11.42 mmol g^{-1} h^{-1} in pure water and 61.96 mmol g^{-1} h^{-1} in isopropanol/water (9:1 v/v). Leveraging the high efficiency, a single-photocatalyst tandem platform generates 22.1 mM H_2O_2, which is subsequently consumed to drive the hydrobromination of 4-methylstyrene with 99% conversion and 87% selectivity, demonstrating the practical utility of in situ photocatalytic H_2O_2. This integrated approach outlines a blueprint for circular, solar-driven photoredox catalysis that upgrades O_2 and H_2O into value-added organic products.

1 | Introduction

Hydrogen peroxide (H_2O_2) is an environmentally benign oxidant and ranks among the top 100 chemicals in global production, with wide applications in propulsion, wastewater treatment, and organic synthesis [1, 2]. The conventional anthraquinone process produces H_2O_2 at an industrial scale but is impractical for decentralized or small-volume needs [3, 4]. In contrast, photocatalytic H_2O_2 generation offers a sustainable, on-demand route for solar-to-chemical energy conversion [5–11]. However, current photocatalytic systems yield only very low concentrations of H_2O_2, which makes in-situ separation and enrichment difficult, severely restricting direct utilization [12, 13]. This concentration bottleneck poses a significant challenge for the practical deployment of solar H_2O_2 production.

A promising solution for the low-concentration issue is to directly convert the generated H_2O_2 into valuable hydrophobic organic products in the same reaction vessel. This tandem approach couples the photocatalytic reduction of O_2 to H_2O_2 with an immediate photocatalytic oxidation of an organic substrate on a single catalyst, thereby eliminating the need to isolate H_2O_2. By integrating two photoredox processes into one system, the approach streamlines H_2O_2 utilization and significantly reduces

Qiang Xue, Jiehua Ding, and Zhendong Luo contributed equally to this work.

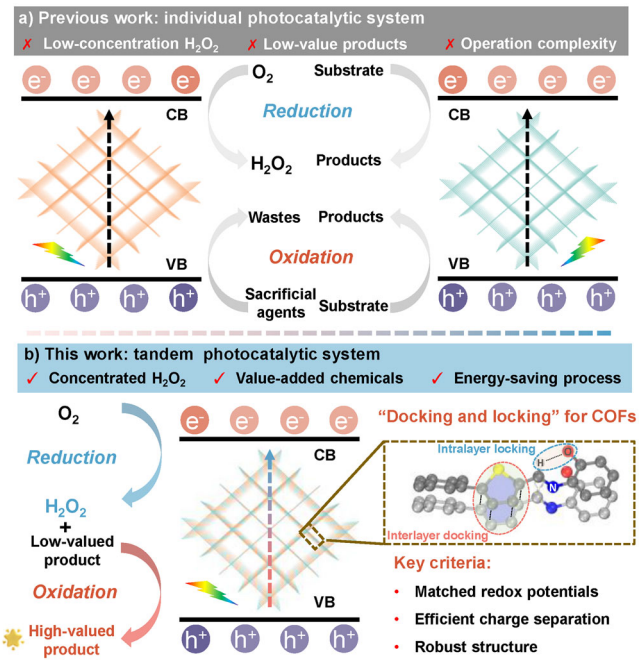

FIGURE 1 | Molecular design of docking and locking COFs. (a) Previous work for an individual photocatalytic system. (b) Tandem photocatalytic system for this work.

processing complexity and cost. Implementing such a one-pot tandem transformation requires carefully engineered photocatalyst that meets several key criteria: (i) Thermodynamically matched redox potentials for both H_2O_2 production and the target photoredox reaction (ensuring both processes are energetically feasible); (ii) Sufficient driving force (e.g., strong light absorption and efficient charge separation) to sustain high photocatalytic activity through both stages of the reaction; (iii) Robust structural stability under combined reaction conditions throughout the two-step process.

Covalent organic frameworks (COFs), with their well-defined π-conjugated skeletons, tunable optoelectronic properties, and periodic porous networks, show great promise for meeting these criteria and provide an excellent platform for both photocatalytic H_2O_2 production and organic transformations [14–21]. However, most previous efforts have focused on optimizing individual reactions for either H_2O_2 generation or organic oxidation [22–27], without addressing the intrinsic compatibility required to couple both processes in one system (Figure 1a). The major reason lies in the relatively low chemical stability and limited conjugation degree of many COFs, which compromise structural robustness and hinder efficient charge separation, thereby restricting their suitability for one-pot reactions. This gap highlights the need for a new design strategy to enable a single COF material to carry out consecutive H_2O_2 generation and follow-up organic reactions within the same framework.

In this work, a "docking and locking" strategy is developed for COF photocatalysts to successfully realize one-pot tandem transformation. This approach integrates interlayer docking units, which prevent interlayer slippage and enhance structural stability [28], with intralayer hydrogen-bond locking, which strengthens π-conjugation and facilitates charge transfer [29–31]. Through the combination of these design elements, the COF framework attains the robustness and electronic alignment necessary to directly convert low-concentration H_2O_2 to hydrophobic organic products in a single system (Figure 1b). Using this strategy, we constructed a series of thiophene-based COFs with interlayer docking units and evaluated them for photocatalytic H_2O_2 production. Among them, TTPh-OH, which benefits from strong hydrogen-bond-induced intralayer locking, exhibits the highest activity, achieving an H_2O_2 production rate of 11.42 mmol g^{-1} h^{-1}. Remarkably, in the presence of a sacrificial isopropanol/water (9:1 v/v) mixture, the H_2O_2 generation rate of TTPh-OH surges to 61.96 mmol g^{-1} h^{-1}, far surpassing most reported COF-based photocatalysts. Building on this high activity, a single-catalyst tandem system integrating in situ H_2O_2 synthesis with value-added organic transformation is established. In Stage I, the COF photocatalyst accumulates an H_2O_2 concentration of 22.1 mM (IPA:H_2O = 9:1) over 10 h of visible-light irradiation. In Stage II, the in-situ generated H_2O_2 immediately drives the hydrobromination of 4-methylstyrene in the same vessel, achieving ~99% substrate conversion with 87% selectivity within 1 h. Collectively, this atom-economical platform provides a blueprint for direct solar-driven conversion of O_2/H_2O into high-value organics, opening new opportunities for sustainable chemical manufacturing.

2 | Results and Discussion

1,2,4,5-tetrayl-(thiophene-2-carbaldehyde)-phenebenzene (TTPh) units are designed with a twisted, noncoplanar conformation (dihedral angle 44~55°), creating propeller-shaped docking sites that interlock adjacent layers (Figure 2a). Thiophene motifs serve as high-performance building blocks due to their tunable energy levels and efficient charge separation arising from abundant lone-pair electrons [32]. To systematically modulate the π-conjugation of the framework, biphenyl linkers with different substituents are incorporated. Condensation of TTPh with these linkers through Schiff-base chemistry produces a series of curved, quadrilateral COFs, denoted TTPh-X (X = OH, Me, or H) (Figure 2b). Among them, the hydroxyl-functionalized linker forms intralayer hydrogen bonds with the imine linkages, generating an intralayer "locking" effect that enhances structural planarity and yields the strongest π-conjugation (Figure 2c–e). To provide a quantitative assessment of the docking extent, the root mean square deviation (RMSD) analysis of adjacent layers confirms excellent geometric rigidity and a high degree of three-dimensional spatial alignment, with values of 0.16, 0.36, and 0.25 Å for TTPh-OH, TTPh-CH_3, and TTPh-H, respectively (Figure S1).

Powder x-ray diffraction (PXRD) patterns confirm the high crystallinity of all synthesized COFs. The experimental patterns show excellent agreement with the simulated ones, along with low refinement agreement factors (Figures 2f, S2, and S3; Tables S1–S3). TTPh-OH displays sharp diffraction peaks at 2θ = 4.07°, 5.79°, 8.11°, and 12.67°, indexed to the (100), (110), (020), and (030) planes, respectively. These features are fully consistent with the simulated SQL topology rather than the kgm model (Figure S4). In addition, comparative analysis of the three materials under distinct stacking models further confirms their structural uniformity and the presence of a well-defined AA stacking mode

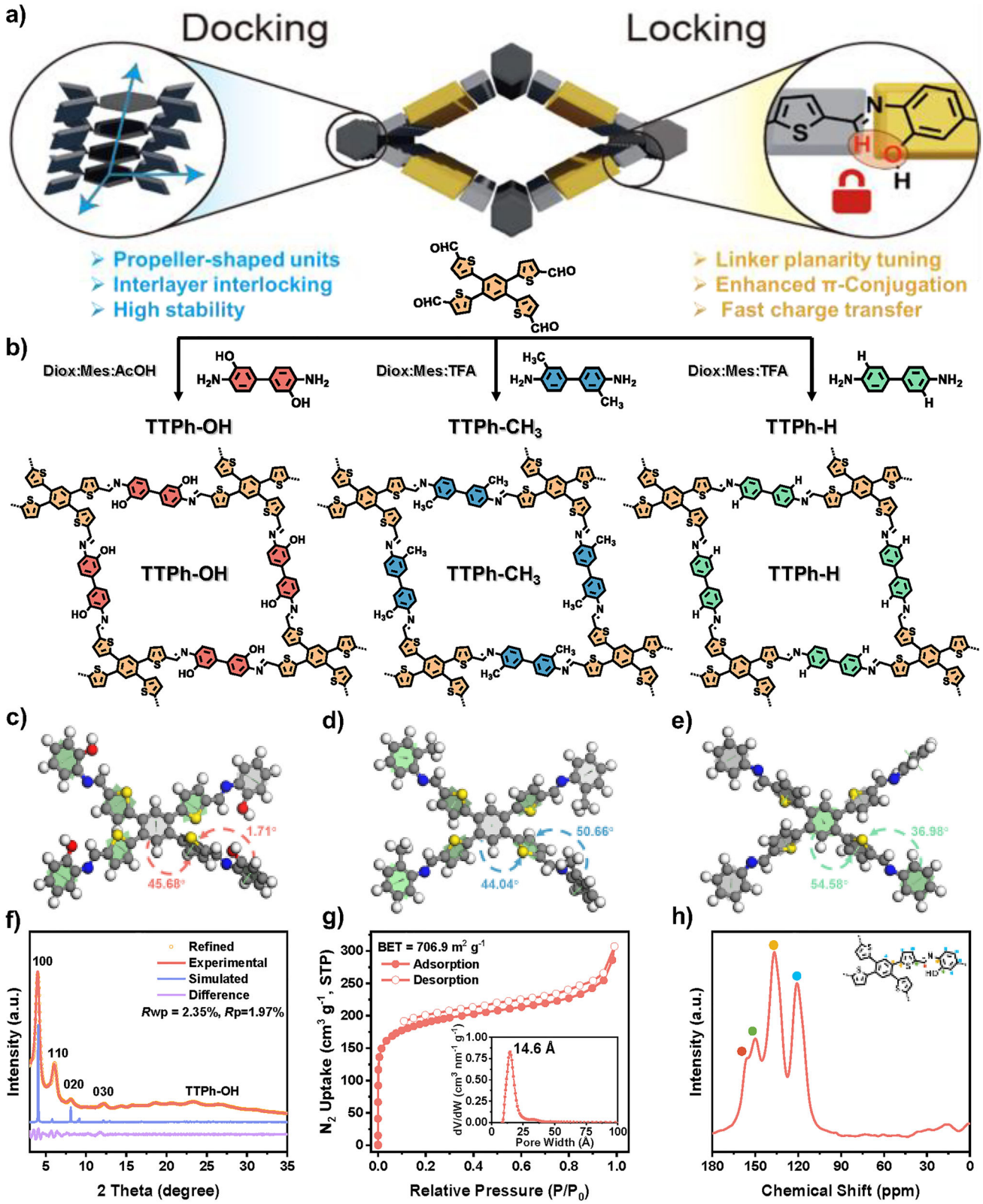

FIGURE 2 | Chemical, crystal, and geometric structures. (a) Docking and locking concept and structural characterization of TTPh-based COFs. (b) Schematic illustration for the synthesis of three COFs. (c–e) Enlarged local structural motifs of TTPh-OH (c), TTPh-CH_3 (d), and TTPh-H (e), showing dihedral twisting at docking sites and coplanarity regulation along the linkers at locking sites. (f) PXRD patterns of TTPh-OH. (g) The BET Plot of TTPh-OH at 77 K and pore size distribution curve. (h) The solid state ^{13}C-NMR spectra of TTPh-OH.

(Figures S5–S7). Owing to the interlayer docking effect, TTPh-OH also shows remarkable robustness: its PXRD pattern remains unchanged after 3 days in strong acid (1 M HCl), base (1 M NaOH), and various organic solvents, including NMP, MeOH, THF, CH_3CN, EtOH, and IPA (Figure S8). Together with its thermal stability up to 400°C (Figure S9), these properties establish TTPh-OH as a structurally and chemically durable platform for photocatalytic H_2O_2 generation and organic transformations.

Nitrogen sorption measurements show typical type-I isotherms, confirming the porous nature of all COFs. The BET surface areas of TTPh-OH, TTPh-CH_3, and TTPh-H are 707, 655, and 562 $m^2\ g^{-1}$, with corresponding pore sizes of 14.6, 15.6, and 15.9 Å (Figures 2g, S10, and S11). These values agree well with the simulated structures, verifying the successful synthesis of the desired frameworks. Fourier-transform infrared (FT-IR) spectra display the characteristic C═N stretching band at ~1620 cm^{-1} and the disappearance of the N–H band at ~3279 cm^{-1}, indicating complete imine condensation (Figures S12–S14). Solid-state ^{13}C NMR further confirms the formation of C═N linkages, showing resonances at 157–160 ppm, while diagnostic signals for C–OH (150 ppm) and -CH_3 (20 ppm) appear in TTPh-OH and TTPh-CH_3, respectively (Figures 2h, S15, and S16). Morphologically, scanning electron microscopy (SEM) reveals petal-like TTPh-OH, smooth-sheet TTPh-CH_3, and rod-like TTPh-H (Figure S17). High-resolution transmission electron microscopy (HR-TEM) further visualizes ordered lattice fringes and layered frameworks in all samples (Figures S18–S20).

Photoelectrochemical analyses evaluate the charge-separation efficiency in TTPh-X. TTPh-OH shows a markedly higher transient photocurrent response than its analogs (Figure 3a), and its Nyquist semicircle radius is the smallest among them (Figure S21), indicating faster charge-transfer kinetics. Time-resolved photoluminescence (TRPL) spectra further support this conclusion: TTPh-OH displays the longest carrier lifetime (Figure 3b and Table S4), consistent with suppressed recombination and prolonged charge separation in photocatalysis.

To gain further insights into the electron-transfer processes involved, ultrafast transient absorption (TA) spectroscopy is employed as a powerful tool to probe real-time photoexcited carrier dynamics in COF systems. All three COFs display a well-defined excited-state absorption (ESA) band centered at ~458 nm (Figures S22–S24). Kinetic analysis of this ESA feature reveals two characteristic decay components: τ_1, associated with the ultrafast localization of conduction-band electrons into bound excitons, and τ_2, corresponding to the subsequent electron–hole recombination [33]. TTPh-OH exhibits the shortest τ_1 (188.377 ns), indicating the strongest exciton binding, and the longest τ_2 (1217.79 ns), reflecting the slowest recombination rate (Figure 3c). Consequently, TTPh-OH achieves the longest average carrier lifetime (1180.28 ns), which is approximately 1.6- and 3.8-fold longer than those of TTPh-CH_3 and TTPh-H, respectively (Figures S23c and S24c). These results demonstrate that enhanced exciton stabilization in TTPh-OH effectively suppresses ultrafast recombination.

This trend can be confirmed by the calculated three-dimensional charge-transport characteristics derived from the electron and hole effective masses (m_e*, m_h*). Within the layers, TTPh–OH displays markedly lower effective masses (m_e* = 1.307, m_h* = 2.692) than its counterparts (Figures 3d-f S25, and S26), indicating higher carrier mobility and more efficient charge migration attributed to its enhanced π-conjugation along the linker. Furthermore, DFT calculations are carried out to quantitatively evaluate the charge-transfer capability [34]. For the ground state, TTPh–OH shows the largest charge transfer (~0.82 |e|) from donor (TTPh linker) to acceptor units (biphenyl linker), whereas TTPh–H exhibits a smaller transfer (~0.56 |e|), consistent with the Photoelectrochemical analyses (Figure S27). High-resolution XPS spectra of C 1s and N 1s further substantiate the distinct charge-transfer characteristics between donor and acceptor units (Figure S28). In TTPh–OH, the thiophene C–S bond belonging to the donor component shifts to the highest binding energy (BE), while the –C═N– peak associated with the acceptor unit appears at the lowest BE among the three COFs. These shifts indicate an intensified built-in electric field (BIEF) in TTPh–OH that facilitates more efficient in-plane charge transfer. In contrast, TTPh–CH_3 and TTPh–H exhibit attenuated BIEF strengths, reflecting reduced electron delocalization within the donor moieties. Time-dependent DFT calculations using CP2K visualize the spatial distributions of photoexcited electrons and holes in the three COFs (Figure 3g–i) [35, 36]. The calculated orbital overlap integral (Sr), which reflects the degree of wavefunction overlap between ground and excited states, follows the order TTPh-CH_3 (0.268) < TTPh-H (0.462) < TTPh-OH (0.635). The highest Sr value for TTPh-OH indicates stronger electronic coupling that promotes efficient charge excitation. Conversely, the centroid distance (D) between electron and hole densities decreases in the reverse order—TTPh-OH (2.506 Å) > TTPh-CH_3 (0.897 Å) > TTPh-H (0.572 Å)—suggesting enhanced charge separation and prolonged carrier lifetimes in TTPh-OH, consistent with TRPL and TA observations [37]. These results highlight the synergistic combination of efficient charge excitation and suppressed recombination in TTPh-OH arising from the intralayer "locking" effect. Subsequently, the energy levels of TTPh-X are evaluated. TTPh-OH exhibits a pronounced redshift in its absorption edge to ~700 nm (Figure S29a), corresponding to a narrower bandgap (1.90 eV) than TTPh-CH_3 (2.18 eV) and TTPh-H (2.12 eV) (Figure S29b), indicative of enhanced π-conjugation arising from the intralayer "locking" effect. All three COFs display n-type behavior, as indicated by the positive slopes of their Mott–Schottky (M–S) plots. With flat-band potentials of –0.78, –0.82, and –0.67 V versus Ag/AgCl for TTPh-OH, TTPh-CH_3, and TTPh-H, respectively (Figures S30–S32), the derived conduction and valence-band positions confirm that each COF offers sufficient thermodynamic driving force for both oxygen reduction and water oxidation to O_2 (Figure 3j) [38]. Together, these results confirm the thermodynamic feasibility of photocatalytic H_2O_2 production.

To evaluate the photocatalytic H_2O_2 production efficiency of the COFs under ambient conditions, the materials are dispersed in water and saturated with O_2 for 30 min before visible-light irradiation (λ > 420 nm, 20°C) (Figures S33 and S34). The H_2O_2 formation rates follow the order TTPh-OH (11.42 mmol $g^{-1}\ h^{-1}$) > TTPh-CH_3 (5.89 mmol $g^{-1}\ h^{-1}$) > TTPh-H (3.21 mmol $g^{-1}\ h^{-1}$) (Figure 4a), underscoring the superior activity of TTPh-OH. To decouple the structural "locking" effect from the inherent electron-donating property of the –OH group, a control COF (TTPh-OCH_3, Figure S35) was synthesized. Its

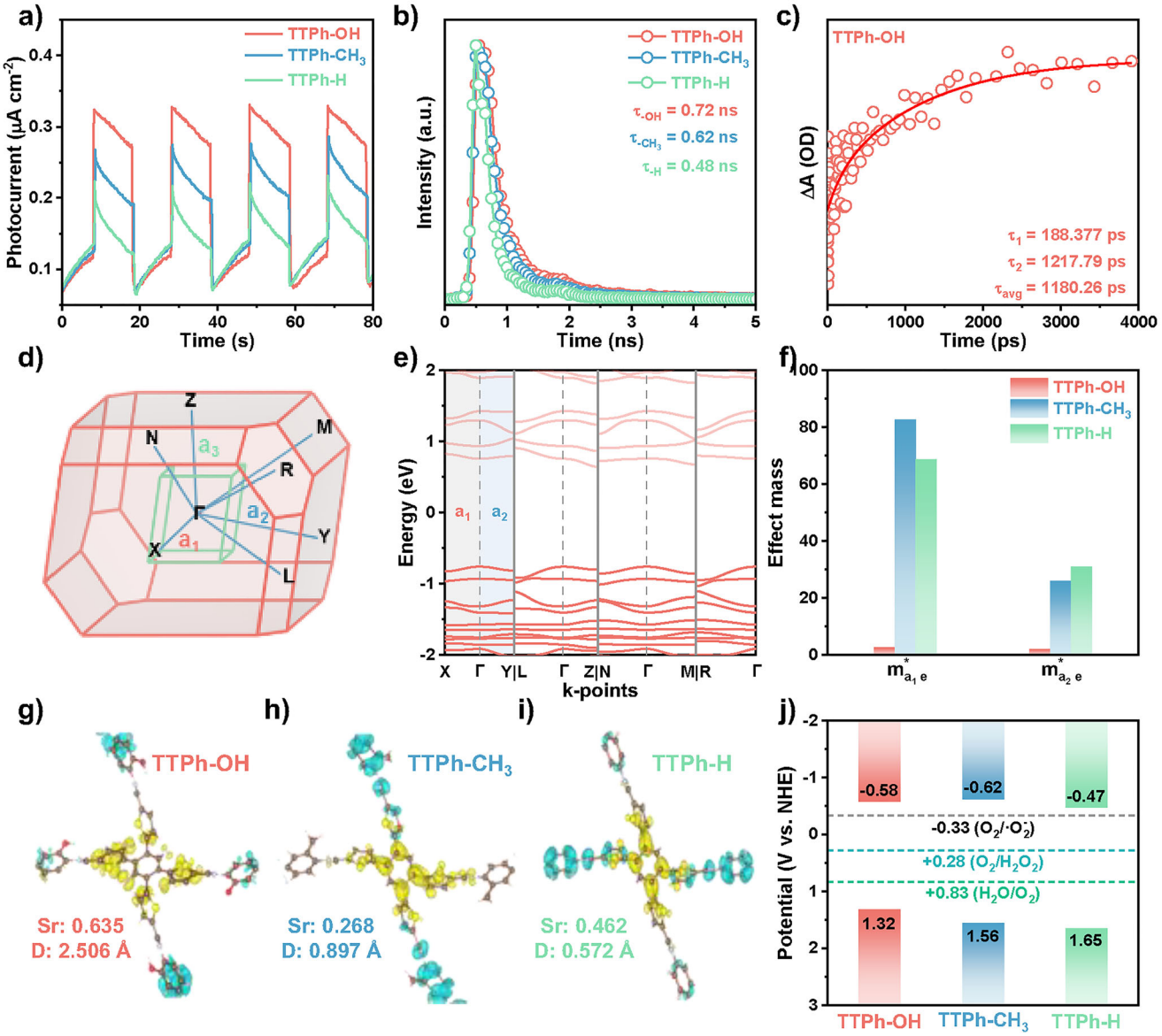

FIGURE 3 | Photophysical and electrochemical properties. (a) Transient photocurrent response. (b) Time-resolved transient PL decay curves of TTPh-OH TTPh-CH_3, and TTPh-H. (c) fs-TA spectra of TTPh–OH at selected delay times under 450 nm excitation. (d) Brillouin zone of the Triclinic (TRI) lattice. Path: X-Γ-Y|L-Γ-Z|N-Γ-M|R-Γ. (e) Theoretical calculation band structure of TTPh-OH. (f) electron effective masses (me*) along intralayer directions (a_1, a_2). (g–i) Time-dependent DFT (TD-DFT) derived spatial distributions of excited electrons (blue) and holes (yellow) for TTPh-OH (g), TTPh-CH_3 (h), and TTPh-H (i). (j) Energy band structures corresponding to the three types of COFs.

significantly lower photocatalytic activity, which is comparable to the non-hydroxylated analogs, combined with theoretical analysis, confirms that the performance enhancement is predominantly attributable to the interlayer docking and locking mechanism rather than electronic effects. Furthermore, the solvent composition markedly influences performance (Figure 4b). Using TTPh-OH as the catalyst, the H_2O_2 generation rates reach 11.69 mmol g^{-1} h^{-1} (MeOH:H_2O = 9:1), 26.60 mmol g^{-1}·h^{-1} (IPA:H_2O = 1:1), 38.75 mmol g^{-1} h^{-1} (EtOH:H_2O = 9:1), and 61.96 mmol g^{-1} h^{-1} (IPA:H_2O = 9:1). Control experiments confirm that neither light nor catalyst alone produces detectable H_2O_2 (Figure S36), verifying the photocatalytic origin of the reaction. TTPh-OH consistently maintains high activity in both aqueous and alcoholic media, outperforming most reported COF photocatalysts (Figure 4c and Table S5). The apparent quantum yield reaches 2.3% at 425 nm and decreases at longer wavelengths (Figure S37). A solar-to-chemical conversion (SCC) efficiency of 0.45% is achieved—over four times that of natural photosynthesis (~0.1% in plants). The material also shows excellent cycling stability, retaining crystallinity (XRD) and chemical integrity (FT-IR) after repeated use (Figures S38 and S39). Linear sweep voltammetry (LSV) tests further confirm enhanced current density, a lower onset potential, and superior H_2O_2 selectivity (70%) for TTPh-OH (Figure S40). Collectively, these results establish TTPh-OH as the most efficient and selective photocatalyst among the TTPh-X series, consistent with its favorable photophysical and electrochemical characteristics.

To elucidate the reaction mechanism, H_2O_2 formation is evaluated under various atmospheres. Lower yields under air and

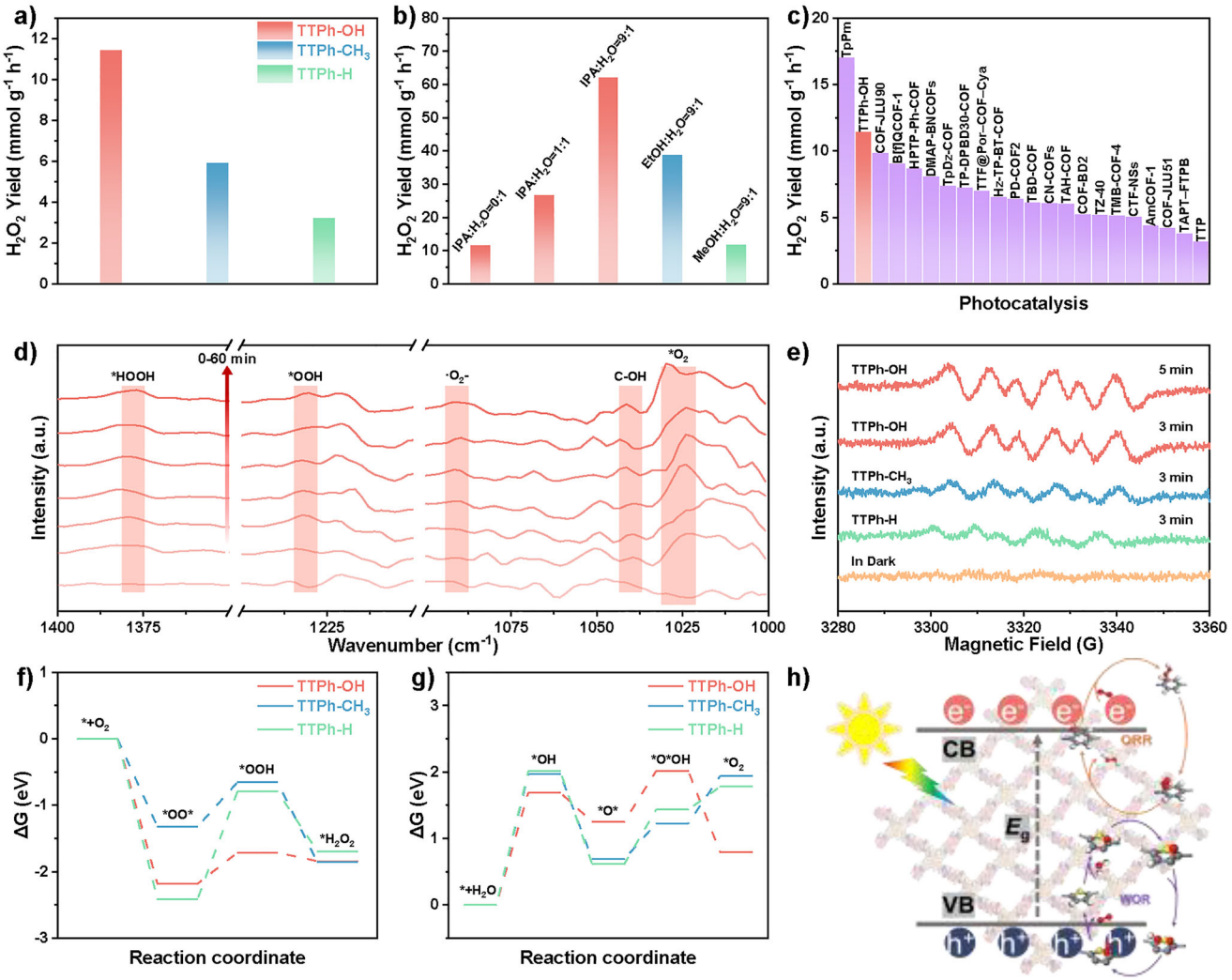

FIGURE 4 | H_2O_2 Photosynthesis and in-situ mechanism. (a) Photocatalytic H_2O_2 production yield for TTPh-OH, TTPh-CH_3 and TTPh-H. (b) Photocatalytic H_2O_2 production yield of TTPh-OH under different solvents. (c) Comparison of H_2O_2 production rates of TTPh-OH with previously reported COF-based photocatalysts in pure water. (d) DRIFTS study of TTPh-OH collected at different photoirradiation times under O_2 and H_2O vapor from 1000–1400 cm^{-1}. (e) EPR spectra of DMPO-$\cdot O_2^-$ adducts in methanol dispersions of different COFs. (f, g) Gibbs free-energy profiles for the ORR (f) and WOR (g) on TTPh–OH, TTPh–CH_3, and TTPh–H. (h) Schematic illustration of the photocatalytic mechanisms for H_2O_2 production over TTPh-OH in pure water.

nearly no activity under Ar confirm the essential role of O_2 (Figure S41). Radical-trapping experiments further show that quenching superoxide radicals ($\cdot O_2^-$) with nitro blue tetrazolium (NBT) or photogenerated electrons with $AgNO_3$ markedly suppresses H_2O_2 generation, whereas tert-butanol ($\cdot$OH scavenger) exhibits negligible influence (Figure S42). Electron paramagnetic resonance (EPR) spectra using DMPO as a spin-trapping agent reveal strong $\cdot O_2^-$ signals for TTPh-OH under illumination, while only weak signals appear for TTPh-CH_3 and TTPh-H, and no signal is detected in the dark (Figure 4e). Therefore, photosynthesis of H_2O_2 primarily arises from two consecutive single-electron reduction steps, while the oxidation half-reaction does not contribute to its generation. Rotaing ring-disk electrode (RRDE) tests under Ar atmosphere show disk current only at −0.3 V (vs. Ag/AgCl), indicative of O_2 rather than H_2O_2 evolution (Figure S43). Furthermore, an $H_2{}^{18}O$ isotope-labeling experiment confirms the evolved O_2 originates from the water-oxidation reaction (WOR): $^{18}O_2$ is detected in the gas phase and identified after MnO_2-assisted decomposition, directly linking WOR-derived O_2 to the subsequent oxygen reduction reaction (ORR) responsible for producing H_2O_2 (Figures S44 and S45).

In situ diffuse reflectance infrared Fourier transform spectroscopy (DRIFTS) offers additional mechanistic insight by monitoring the evolution of key reaction intermediates (Figure 4d). A growing signal at 1187 cm^{-1} is assigned to $\cdot O_2^-$ [39], consistent with the spin-trapping results. Signals corresponding to **OO** (1025 cm^{-1}), **OOH** (1230 cm^{-1}), and **HOOH** (1325 cm^{-1}) sequentially appear [40], confirming a proton-coupled electron-transfer (PCET) cascade from **OO** to HOOH. The emergence of a C–OH vibration at 1090 cm^{-1} further indicates the concurrent WOR progress [41]. Furthermore, DFT calculations are performed to elucidate the catalytic mechanism of photocatalytic H_2O_2 synthesis (Figures 4f,g). In the ORR process, TTPh-OH shows the lowest Gibbs free-energy barrier (0.47 eV) for the **OO*→*OOH* step, which corresponds to the PCET process regarded as the

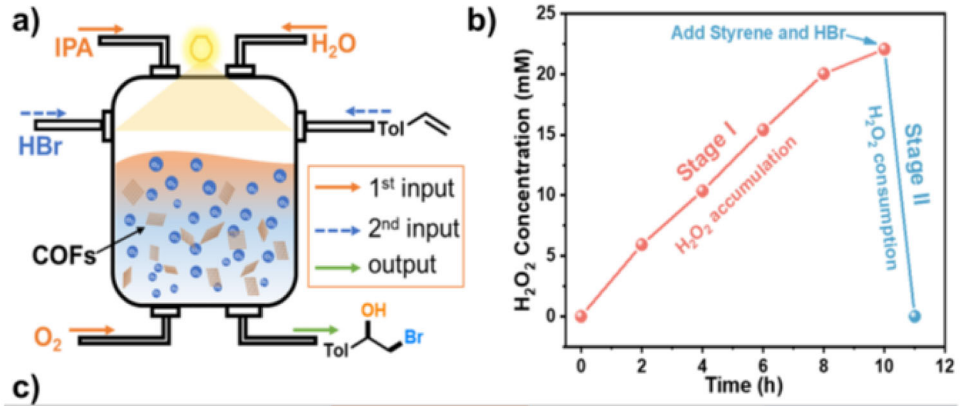

c)

Entry	Reactant	Conversion	Product	Selectivity
1	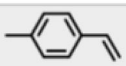	99%	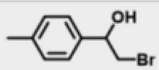	87%
2	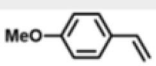	99%	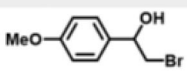	65%
3	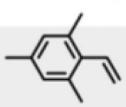	83%	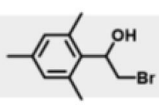	90%
4	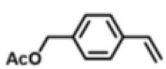	66%	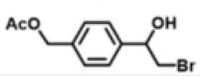	55%
5	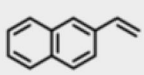	93%	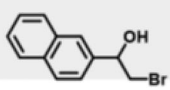	50%
6	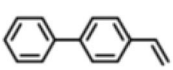	92%	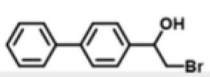	90%
7	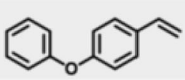	76%	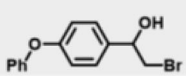	86%
8	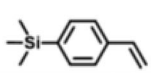	66%	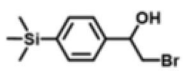	80%
9	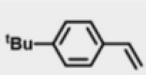	81%	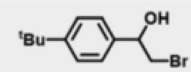	73%
10	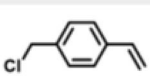	65%	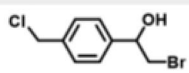	91%
11	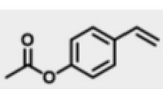	65%	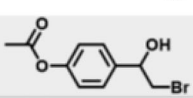	86%

FIGURE 5 | Hydrobrominated products by tandem catalytic reaction and substrates screening. (a) Schematic illustration of the one-pot, two-stage solar-driven conversion of O_2 and H_2O into H_2O_2 and its in situ utilization on the same TTPh-OH photocatalyst without further separation and extraction. (b) Time-dependent H_2O_2 concentration: stage I, photocatalytic generation of H_2O_2 by TTPh-OH (25 mg) in isopropanol/H_2O (9:1 v/v, 50 mL) mixed solvent under 10 h of irradiation; Stage II, consumption of the generated H_2O_2 after the addition of styrene and HBr. (c) Product yields and selectivities in styrene functionalization.

rate-determining step. For the WOR process, TTPh-OH displays the most favorable energetics for the generation of *OH [42, 43]. These results collectively demonstrate that the hydroxyl substituent optimizes charge dynamics and intermediate stabilization, thereby lowering reaction barriers across both ORR and WOR pathways and underpinning the exceptional photocatalytic activity of TTPh-OH (Figure 4h).

Current photocatalytic H_2O_2 production systems are largely confined to environmental remediation or bacterial disinfection [44, 45]. Given exceptional activity and durability of TTPh-OH for O_2-to-H_2O_2 conversion (Figures S34–S36), we sought to extend its utility toward in situ photocatalytic upgrading of H_2O_2 into value-added organics. To emulate industrial processes and minimize operational complexity [46–48], a one-pot tandem photocatalytic

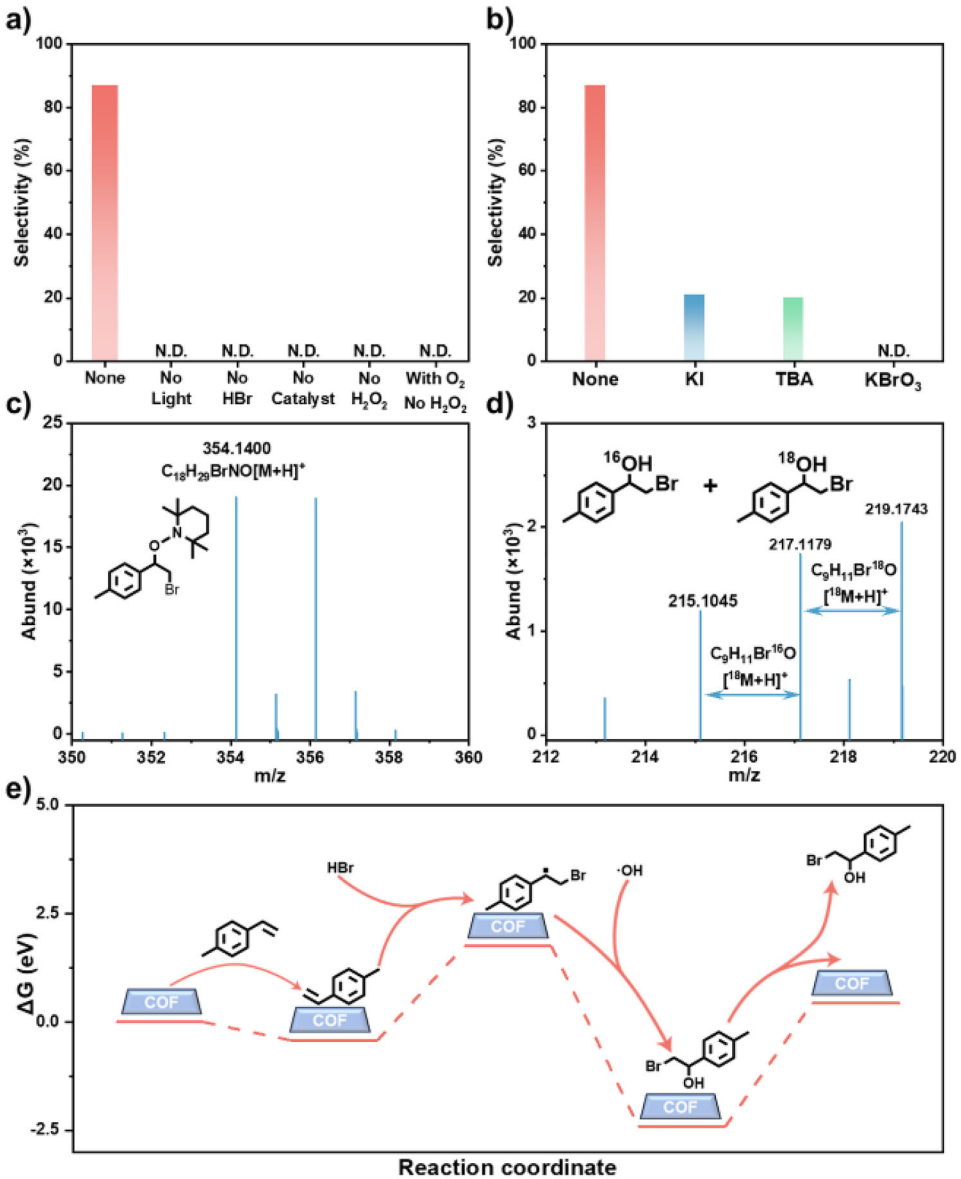

FIGURE 6 | Control, trapping, and theoretical studies. (a) Control experiments were performed in the absence of light, catalyst, HBr, or H_2O_2. (b) Reaction selectivity in Stage II in the presence of different radical-trapping reagents. (c) TEMPO-trapping of reaction intermediates during stage II. (d) An isotopic-labeling experiment confirming the oxygen source. (e) Gibbs free energy diagram and proposed reaction pathway for the photocatalytic alkene bifunctionalization.

system comprising two stages: (1) photocatalytic H_2O_2 generation and accumulation, and (2) additive-assisted photocatalytic H_2O_2 utilization. This cascade directly converts O_2 and H_2O into a functional oxidant (H_2O_2) in situ, bypassing any intermediate isolation (Figure 5a). Bromohydrins constitute a versatile group of organic compounds, frequently employed as pivotal synthons in the preparation of diverse bioactive molecules with high value. Owing to their chemical versatility, these compounds can be efficiently transformed into a range of pharmacologically relevant structures, including epoxides, aminoalcohols, and aziridines, all of which are essential building blocks in medicinal chemistry [49–51]. As a demonstration, we integrate TTPh-OH-driven H_2O_2 synthesis with alkene hydrobromination, replacing the conventional hazardous bromine sources (e.g., bromate, N-bromoimides) and costly oxidants (e.g., metal salts, Oxone) [52, 53]. Under visible-light irradiation ($\lambda > 420$ nm) at 20°C with O_2 bubbling, TTPh-OH (25 f) in an IPA/ H_2O (9:1 v/v, 50 mL) mixture produces 22.1 mM H_2O_2 after 10 h (Stage I, Figure 5b). Subsequently, upon adding 4-methylstyrene (0.3 mmol) and aqueous HBr (48 wt%, 250 μL) and continuing illumination (Stage II), the reaction yields 2-bromo-1-(p-tolyl)ethan-1-ol (entry 1), achieving 99% conversion with 87% selectivity, and the H_2O_2 was completely consumed within 1 h.

We further explore the generality of this tandem system across various alkenes. A broad range of alkenes was achieved efficient hydrobromination under these conditions, with conversions of 65%–99% and product selectivities of 50%–91% (Figures 5c and S46). Electron-deficient acetates (entries 4 and 11) exhibit reduced activity, while electron-rich substrates (entries 2 and 5) undergo competing Friedel–Crafts bromination. Sterically hindered alkenes (entries 3, 8, and 5) retained high selectivity (73%–90%). Collectively, the broad substrate scope demonstrated

in Figure 5c, together with the elucidated radical mechanism, highlights TTPh-OH as a versatile platform for one-pot tandem photocatalytic transformations and sustainable organic synthesis.

Control experiments confirm that each component—light, TTPh-OH, HBr, and H_2O_2—is indispensable for this transformation (Figure 6a). Furthermore, O_2 alone could not substitute for H_2O_2 in the second stage, underscoring that H_2O_2 acts via a distinct redox pathway (Figure 6a). Mechanistic probes with scavengers reveal that adding KI, TBA, or $KBrO_3$ each markedly suppresses the reaction, indicating the involvement of photogenerated holes, ·OH radicals, and electrons, respectively, in the catalytic cycle (Figure 6b). Consistently, introducing the radical trap TEMPO allows detection of a β-brominated benzyl radical intermediate by liquid chromatography–mass spectrometry (LC–MS) (Figure 6c). An isotopic labeling experiment with 10 vol% $H_2{}^{18}O$ added in Stage II yields an ~1:1 mixture of ^{16}O- and ^{18}O-labeled product, indicating that ^{16}OH generated from $H_2{}^{16}O_2$ undergoes rapid hydrogen-atom transfer with $H_2{}^{18}O$ (Figure 6d). Based on these insights, the mechanism of in situ H_2O_2 upgrading has been proposed: under illumination, photogenerated holes oxidize Br^- to ·Br radicals, which add to the alkene to form β-brominated carbon radicals; concurrently, the photo-reduced H_2O_2 produces ·OH radicals that couple with these intermediates to yield the corresponding bromohydrin alcohols (Figure 6e). This concerted radical-mediated process thus exemplifies a solar-driven, atom-economical strategy to valorize H_2O_2 into value-added organic chemicals.

3 | Conclusion

In summary, this work demonstrates that a molecular "docking and locking" strategy enables COF photocatalysts to achieve robust structural integrity and finely tuned electronic properties required for one-pot tandem transformations. By combining interlayer docking units that prevent layer slippage with intralayer hydrogen-bond locking that enhances π-conjugation and charge transfer, the resulting COF framework (TTPh–OH) exhibits outstanding photocatalytic performance, achieving H_2O_2 generation rates of up to 61.96 mmol g^{-1} h^{-1} and enabling its direct in situ upgrading through a single-photocatalyst tandem process. This atom-economical process not only demonstrates the feasibility of coupling oxidative and reductive photocatalysis in a unified COF platform, but also provides a molecular blueprint for designing next-generation photocatalysts capable of converting ubiquitous feedstocks, O_2, and H_2O, into value-added chemicals through sustainable, circular photoredox chemistry.

Acknowledgments

This work was financially supported by the National Natural Science Foundation of China (No. 22301298 and 22405258), Open Fund of State Key Laboratory of Catalysis (No. 2024SKL-A-007), Liaoning Revitalizing Talents Program (No. XLYC2403136), Natural Science Foundation Youth Project of Anhui Province (2408085QB070), the Postdoctoral Fellowship Program of CPSF under Grant Number (GZB20240723), the Fundamental Research Funds for the Central Universities (WK9990250187), the startup funds from Dalian Institute of Chemical Physics and Chinese Academy of Sciences. We also thank the instrumental support of the Liaoning Key Laboratory of Biomass Conversion for Energy and Material.

Conflicts of Interest

The authors declare no conflicts of interest.

Data Availability Statement

The data that support the findings of this study are available in the Supporting Information of this article.

References

1. Y. Shiraishi, T. Takii, T. Hagi, et al., "Resorcinol–Formaldehyde Resins as Metal-Free Semiconductor Photocatalysts for Solar-to-Hydrogen Peroxide Energy Conversion," *Nature Materials* 18 (2019): 985–993, https://doi.org/10.1038/s41563-019-0398-0.

2. Y. Chen, R. Liu, Y. Guo, et al., "Hierarchical Assembly of Donor–Acceptor Covalent Organic Frameworks for Photosynthesis of Hydrogen Peroxide From Water and Air," *Nature Synthesis* 3 (2024): 998–1010, https://doi.org/10.1038/s44160-024-00542-4.

3. T. Freese, J. T. Meijer, B. L. Feringa, and S. B. Beil, "An Organic Perspective on Photocatalytic Production of Hydrogen Peroxide," *Nature Catalysis* 6 (2023): 553–558, https://doi.org/10.1038/s41929-023-00980-x.

4. S. J. Freakley, Q. He, J. H. Harrhy, et al., "Palladium-tin Catalysts for the Direct Synthesis of H_2O_2 With High Selectivity," *Science* 351 (2016): 965–968, https://doi.org/10.1126/science.aad5705.

5. C. Krishnaraj, H. Sekhar Jena, L. Bourda, et al., "Strongly Reducing (Diarylamino)Benzene-Based Covalent Organic Framework for Metal-Free Visible Light Photocatalytic H_2O_2 Generation," *Journal of the American Chemical Society* 142 (2020): 20107–20116, https://doi.org/10.1021/jacs.0c09684.

6. Z. Zhang, Y. Qian, and H.-L. Jiang, "Photocatalytic Overall Reacttions over MOFs and COFs," *Chem* 12 (2026): 102778, https://doi.org/10.1016/j.chempr.2025.102778.

7. W. Zhao, P. Yan, B. Li, et al., "Accelerated Synthesis and Discovery of Covalent Organic Framework Photocatalysts for Hydrogen Peroxide Production," *Journal of the American Chemical Society* 144 (2022): 9902–9909, https://doi.org/10.1021/jacs.2c02666.

8. Z. Yong and T. Ma, "Solar-to-Catalyzed Covalent Organic Frameworks," *Angewandte Chemie International Edition* 62 (2023): e202308980, https://doi.org/10.1002/anie.202308980.

9. H. Zheng, J. Ji, Y. Yusran, et al., "Three-Dimensional Covalent Organic Frameworks With JCG Topology Based on a Trinodal Strategy," *Journal of the American Chemical Society* 147 (2025): 13667–13676, https://doi.org/10.1021/jacs.5c00961.

10. P. Das, G. Chakraborty, J. Roeser, S. Vogl, J. Rabeah, and A. Thomas, "Integrating Bifunctionality and Chemical Stability in Covalent Organic Frameworks via One-Pot Multicomponent Reactions for Solar-Driven H_2O_2 Production," *Journal of the American Chemical Society* 145 (2023): 2975–2984, https://doi.org/10.1021/jacs.2c11454.

11. C. Feng, J. Luo, C. Chen, et al., "Cooperative Tungsten Centers in Polymeric Carbon Nitride for Efficient Overall Photosynthesis of Hydrogen Peroxide," *Energy & Environmental Science* 17 (2024): 1520–1530, https://doi.org/10.1039/D3EE03032F.

12. H. Ni, Y. Wang, K. Yao, et al., "Cyclical Palmitoylation Regulates TLR9 Signalling and Systemic Autoimmunity in Mice," *Nature Communications* 15 (2024): 1, https://doi.org/10.1038/s41467-023-43650-z.

13. Y. Zhang, C. Pan, G. Bian, et al., "H_2O_2 Generation From O_2 and H_2O on a Near-Infrared Absorbing Porphyrin Supramolecular Photocatalyst," *Nature Energy* 8 (2023): 361–371, https://doi.org/10.1038/s41560-023-01218-7.

14. F. Auras, L. Ascherl, V. Bon, et al., "Dynamic Two-dimensional Covalent Organic Frameworks," *Nature Chemistry* 16 (2024): 1373–1380, https://doi.org/10.1038/s41557-024-01527-8.

15. W. Zhang, Z. Zhong, X. Wei, et al., "Single-Crystal Metal–Organic and Covalent Organic Framework Hybrids Enable Efficient Photoelectrochemical CO_2 Reduction to Ethanol," *Journal of the American Chemical Society* 147 (2025): 17975–17984, https://doi.org/10.1021/jacs.5c03122.

16. A. Natraj, I. R. Landman, C. E. Pelkowski, D. W. Burke, S. Kewalramani, and W. R. Dichtel, "Nonclassical Crystallization Processes of Single-Crystalline Two-Dimensional Covalent Organic Frameworks," *Journal of the American Chemical Society* 146 (2024): 16775–16786, https://doi.org/10.1021/jacs.4c04674.

17. A. Basak, S. Karak, and R. Banerjee, "Covalent Organic Frameworks as Porous Pigments for Photocatalytic Metal-Free C–H Borylation," *Journal of the American Chemical Society* 145 (2023): 7592–7599, https://doi.org/10.1021/jacs.3c00950.

18. C. S. Diercks and O. M. Yaghi, "The Atom, the Molecule, and the Covalent Organic Framework," *Science* 355 (2017): eaal1585, https://doi.org/10.1126/science.aal1585.

19. A. Rodríguez-Camargo, M. W. Terban, M. Paetsch, et al., "Cyclopalladation of a Covalent Organic Framework for Near-Infrared-Light-Driven Photocatalytic Hydrogen Peroxide Production," *Nature Synthesis* 4 (2025): 710–719, https://doi.org/10.1038/s44160-024-00731-1.

20. L. Wang, D. Ma, A. Liu, et al., "Asymmetric Diamine Synthesis for Covalent Organic Frameworks: Boosted Photocatalytic Performance by Restricting β-Ketoenamine Bond Twist," *Angewandte Chemie International Edition* 64 (2025): e202518097, https://doi.org/10.1002/anie.202518097.

21. S. Yang, D. Streater, C. Fiankor, J. Zhang, and J. Huang, "Conjugation- and Aggregation-Directed Design of Covalent Organic Frameworks as White-Light-Emitting Diodes," *Journal of the American Chemical Society* 143 (2021): 1061–1068, https://doi.org/10.1021/jacs.0c11719.

22. M. Lu, S.-B. Zhang, R.-H. Li, et al., "3D Covalent Organic Frameworks With 16-Connectivity for Photocatalytic C(sp^3)–C(sp^2) Cross-Coupling," *Journal of the American Chemical Society* 146 (2024): 25832–25840, https://doi.org/10.1021/jacs.4c08951.

23. H. Guo, S. Wang, X. Chen, et al., "Engineering a Covalent Organic Framework-based Type-II Heterojunction for Enhanced Photocatalytic H_2O_2 Synthesis," *Nature Synthesis* 4 (2025): 1610–1620, https://doi.org/10.1038/s44160-025-00880-x.

24. L. Li, X. Lv, Y. Xue, H. Shao, G. Zheng, and Q. Han, "Custom-Design of Strong Electron/Proton Extractor on COFs for Efficient Photocatalytic H_2O_2 Production," *Angewandte Chemie International Edition* 63 (2024): e202320218, https://doi.org/10.1002/anie.202320218.

25. W. Zhang, M. Sun, J. Cheng, X. Wu, and H. Xu, "Regulating Electron Distribution in Regioisomeric Covalent Organic Frameworks for Efficient Solar-Driven Hydrogen Peroxide Production," *Advanced Materials* 37 (2025): 2500913, https://doi.org/10.1002/adma.202500913.

26. H.-H. Sun, Z.-B. Zhou, Y. Fu, et al., "Azobenzene-Bridged Covalent Organic Frameworks Boosting Photocatalytic Hydrogen Peroxide Production From Alkaline Water: One Atom Makes a Significant Improvement," *Angewandte Chemie International Edition* 63 (2024): e202409250, https://doi.org/10.1002/anie.202409250.

27. Y. Peng, L. Yuan, K.-K. Liu, Z.-J. Guan, S. Jin, and Y. Fang, "Photosynthesis of H_2O_2 using Phenothiazine-Based Covalent-Organic Frameworks Mimicking Coenzyme Q," *Angewandte Chemie International Edition* 64 (2025): e202423055, https://doi.org/10.1002/anie.202423055.

28. L. Ascherl, T. Sick, J. T. Margraf, et al., "Molecular Docking Sites Designed for the Generation of Highly Crystalline Covalent Organic Frameworks," *Nature Chemistry* 8 (2016): 310–316, https://doi.org/10.1038/nchem.2444.

29. X. Chen, M. Addicoat, E. Jin, et al., "Locking Covalent Organic Frameworks With Hydrogen Bonds: General and Remarkable Effects on Crystalline Structure, Physical Properties, and Photochemical Activity," *Journal of the American Chemical Society* 137 (2015): 3241–3247, https://doi.org/10.1021/ja509602c.

30. S. Kandambeth, D. B. Shinde, M. K. Panda, B. Lukose, T. Heine, and R. Banerjee, "Enhancement of Chemical Stability and Crystallinity in Porphyrin-Containing Covalent Organic Frameworks by Intramolecular Hydrogen Bonds," *Angewandte Chemie International Edition* 52 (2013): 13052–13056, https://doi.org/10.1002/anie.201306775.

31. Q. Xue, H. Li, P. Jin, X. Zhou, and F. Wang, "Singlet-Oxygen-Driven Cooperative Photocatalytic Coupling of Biomass Valorization and Hydrogen Peroxide Production Using Covalent Organic Frameworks," *Angewandte Chemie International Edition* 64 (2025): e202423368, https://doi.org/10.1002/anie.202423368.

32. H. Bronstein, Z. Chen, R. S. Ashraf, et al., "Thieno[3,2- b]Thiophene–Diketopyrrolopyrrole-Containing Polymers for High-Performance Organic Field-Effect Transistors and Organic Photovoltaic Devices," *Journal of the American Chemical Society* 133 (2011): 3272–3275, https://doi.org/10.1021/ja110619k.

33. J. Qiu, K. Meng, Y. Zhang, et al., "COF/in $_2S_3$ S-Scheme Photocatalyst With Enhanced Light Absorption and H_2O_2 -Production Activity and Fs-TA Investigation," *Advanced Materials* 36 (2024): 2400288, https://doi.org/10.1002/adma.202400288.

34. J. S. Choe, C. Lee, M. J. Kim, G.-G. Lee, J.-H. Shim, and Y. S. Lim, "Bader Net Charge Analysis on Doping Effects of Sb in $SnSe_2$ and Related Charge Transport Properties," *Journal of Applied Physics* 127 (2020): 185706, https://doi.org/10.1063/5.0005948.

35. M. de Wergifosse and S. Grimme, "The eXact Integral Simplified Time-Dependent Density Functional Theory (XsTD-DFT)," *The Journal of Chemical Physics* 160 (2024): 204110, https://doi.org/10.1063/5.0206380.

36. T. Lu and F. Chen, "Multiwfn: A Multifunctional Wavefunction Analyzer," *Journal of Computational Chemistry* 33 (2012): 580–592, https://doi.org/10.1002/jcc.22885.

37. J. Manigrasso, I. Chillón, V. Genna, et al., "Author Correction: Visualizing Group II Intron Dynamics Between the First and Second Steps of Splicing," *Nature Communications* 13 (2022): 1, https://doi.org/10.1038/s41467-021-27699-2.

38. B. Mishra, A. Alam, A. Chakraborty, et al., "Covalent Organic Frameworks for Photocatalysis," *Advanced Materials* 37 (2025): 2413118, https://doi.org/10.1002/adma.202413118.

39. R.-Q. Xia, Z.-N. Liu, Y.-Y. Tang, et al., "In Situ Exfoliation of Covalent Metal-Organic Frameworks for Enhancing Photocatalytic Hydrogen Peroxide Production," *Angewandte Chemie International Edition* 64 (2025): e202514091, https://doi.org/10.1002/anie.202514091.

40. Q. Zhu, L. Shi, Z. Li, G. Li, and X. Xu, "Protonation of an Imine-linked Covalent Organic Framework for Efficient H_2O_2 Photosynthesis under Visible Light up to 700 nm," *Angewandte Chemie International Edition* 63 (2024): e202408041, https://doi.org/10.1002/anie.202408041.

41. P. Wu, F. Du, Q. Xue, et al., "Photothermal-Catalyzed Hydrogen Peroxide Production Enabled by Gold-Organic Frameworks," *Advanced Functional Materials* 36 (2026): 2420941, https://doi.org/10.1002/adfm.202420941.

42. C. Qin, X. Wu, L. Tang, et al., "Dual Donor-Acceptor Covalent Organic Frameworks for Hydrogen Peroxide Photosynthesis," *Nature Communications* 14 (2023): 5238, https://doi.org/10.1038/s41467-023-40991-7.

43. J.-Y. Yue, J.-X. Luo, Z.-X. Pan, et al., "Regulating the Topology of Covalent Organic Frameworks for Boosting Overall H_2O_2 Photogeneration," *Angewandte Chemie International Edition* 63 (2024): e202405763, https://doi.org/10.1002/anie.202405763.

44. Y. Liu, L. Li, Z. Sang, et al., "Enhanced Hydrogen Peroxide Photosynthesis in Covalent Organic Frameworks Through Induced Asymmetric Electron Distribution," *Nature Synthesis* 4 (2025): 134–141, https://doi.org/10.1038/s44160-024-00644-z.

45. Y. Hou, P. Zhou, F. Liu, et al., "Efficient Photosynthesis of Hydrogen Peroxide by Cyano-Containing Covalent Organic Frameworks From

Water, Air and Sunlight," *Angewandte Chemie International Edition* 63 (2024): e202318562, https://doi.org/10.1002/anie.202318562.

46. X. Ma and W. Zhang, "Recent Developments in One-pot Stepwise Synthesis (OPSS) of Small Molecules," *Iscience* 25 (2022): 105005, https://doi.org/10.1016/j.isci.2022.105005.

47. X. Zhou, Y. Xu, and G. Dong, "Deacylation-aided C–H Alkylative Annulation Through C–C Cleavage of Unstrained Ketones," *Nature Catalysis* 4 (2021): 703–710, https://doi.org/10.1038/s41929-021-00661-7.

48. X. Zhou, Y. Xu, and G. Dong, "Olefination via Cu-Mediated Dehydroacylation of Unstrained Ketones," *Journal of the American Chemical Society* 143 (2021): 20042–20048, https://doi.org/10.1021/jacs.1c09587.

49. X. Ge, Y. Mo, G. Xing, et al., "Synthesis, Biological Evaluation and Molecular Modeling of 2-amino-2-phenylethanol Derivatives as Novel β2-adrenoceptor Agonists," *Bioorganic Chemistry* 79 (2018): 155–162, https://doi.org/10.1016/j.bioorg.2018.04.017.

50. A. H. Neilson, ed., *Organic Bromine and Iodine Compounds in the Handbook of Environmental Chemistry* (Springer, 2003).

51. M. J. Dagani, H. J. Barda, T. J. Benya, and D. C. Sanders, *Bromine Compounds in Ullmann's Encyclopedia of Industrial Chemistry* (Wiley-VCH, 2002).

52. A. K. Macharla, R. Chozhiyath Nappunni, and N. Nama, "Regio- and Stereoselective Hydroxybromination and Dibromination of Olefins Using Ammonium Bromide and Oxone®," *Tetrahedron Letters* 53 (2012): 1401–1405, https://doi.org/10.1016/j.tetlet.2012.01.026.

53. J. S. Yadav, B. V. S. Reddy, G. Baishya, S. J. Harshavardhan, C. Janardhana Chary, and M. K. Gupta, "Green Approach for the Conversion of Olefins Into Vic-halohydrins Using N-halosuccinimides in Ionic Liquids," *Tetrahedron Letters* 46 (2005): 3569–3572, https://doi.org/10.1016/j.tetlet.2005.03.108.

Supporting Information

Additional supporting information can be found online in the Supporting Information section.

Supporting File 1: Anie72075-sup-0001-SuppMat.docx.